Characterization of an Fe≡N–NH$_2$ Intermediate Relevant to Catalytic N$_2$ Reduction to NH$_3$

John S. Anderson,[†,§] George E. Cutsail III,[‡,§] Jonathan Rittle,[†,§] Bridget A. Connor,[†] William A. Gunderson,[‡,#] Limei Zhang,*[,†,‖] Brian M. Hoffman,*[,‡] and Jonas C. Peters*[,†]

[†]Division of Chemistry and Chemical Engineering, California Institute of Technology, Pasadena, California 91125, United States
[‡]Department of Chemistry, Northwestern University, 2145 Sheridan Road, Evanston, Illinois 60208, United States

ⓢ Supporting Information

ABSTRACT: The ability of certain transition metals to mediate the reduction of N$_2$ to NH$_3$ has attracted broad interest in the biological and inorganic chemistry communities. Early transition metals such as Mo and W readily bind N$_2$ and mediate its protonation at one or more N atoms to furnish M(N$_x$H$_y$) species that can be characterized and, in turn, extrude NH$_3$. By contrast, the direct protonation of Fe–N$_2$ species to Fe(N$_x$H$_y$) products that can be characterized has been elusive. Herein, we show that addition of acid at low temperature to [(TPB)Fe(N$_2$)][Na(12-crown-4)] results in a new S = 1/2 Fe species. EPR, ENDOR, Mössbauer, and EXAFS analysis, coupled with a DFT study, unequivocally

assign this new species as [(TPB)Fe≡N–NH$_2$]$^+$, a doubly protonated hydrazido(2−) complex featuring an Fe-to-N triple bond. This unstable species offers strong evidence that the first steps in Fe-mediated nitrogen reduction by [(TPB)Fe(N$_2$)][Na(12-crown-4)] can proceed along a distal or "Chatt-type" pathway. A brief discussion of whether subsequent catalytic steps may involve early or late stage cleavage of the N−N bond, as would be found in limiting distal or alternating mechanisms, respectively, is also provided.
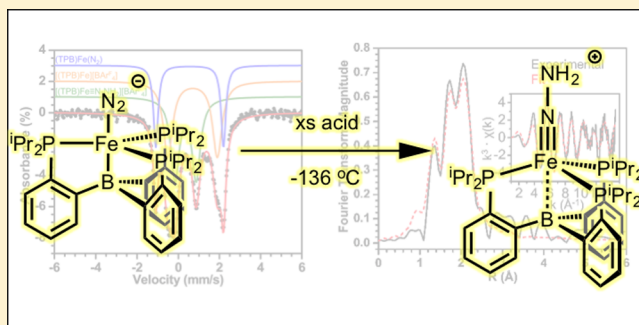
■ INTRODUCTION

Since the discovery[1] and crystallographic characterization[2] of the FeMo-cofactor as the active site of FeMo-nitrogenase, there has been substantial interest in elucidating the mechanism of biological nitrogen reduction.[3] While synthetic model chemistry cannot provide direct mechanistic information regarding enzymatic N$_2$ reduction, it can play a crucial role in exploring the chemical viability of proposed pathways and in exposing new reactivity patterns that help stimulate, frame, and constrain various hypotheses. Early synthetic model work by Chatt, Hidai, and others,[4] as well as recent examples of molecular Mo catalysts for N$_2$ reduction,[5] lent credibility to the initial proposal that the Mo center in the FeMo-cofactor could in principle serve as the site of N$_2$ binding and reduction via a distal or Chatt-type mechanism.[4a,6] More recent spectroscopic, biochemical, and structural studies of FeMo-nitrogenase have suggested that iron is the more likely site for N$_2$ binding and reduction in the FeMo-cofactor.[7] This hypothesis also reflects that, to date, iron is the only transition metal known to be essential to nitrogenase activity, underscored by the characterization of Fe-only nitrogenases.[3b,8] This state of affairs has motivated studies toward the synthesis of Fe complexes that mimic steps in proposed N$_2$ reduction schemes and/or stabilize candidate iron intermediates of biological nitrogen fixation.[9]

Indeed, numerous synthetic studies underscore the idea that an Fe–N$_2$ binding site(s) may be mechanistically relevant to biological N$_2$ fixation.[10] We have been interested in the postulate that a single Fe center can mediate N$_2$ reduction via a flexible ligand environment that enables N$_2$ coordination at Fe and facilitates the stabilization of intermediates exhibiting Fe–N multiple bonding en route to NH$_3$ formation.[11] Isolated synthetic Fe complexes of a tris(phosphine)borane (TPB) scaffold (Scheme 1) with bound N$_2$ or imido (NR$^{2−}$) ligands
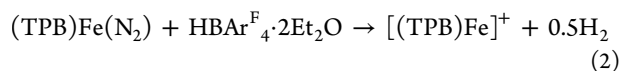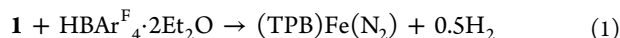
Scheme 1
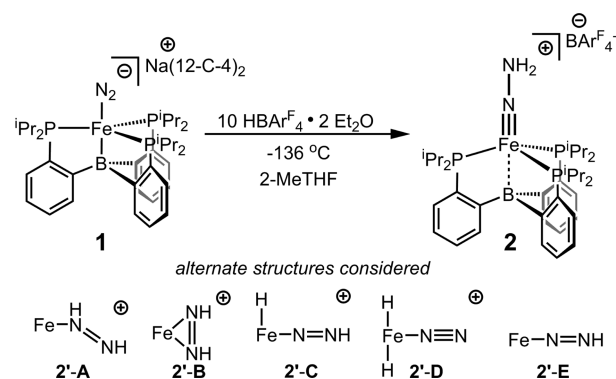
demonstrate important aspects of this single-site hypothesis.[11e,f] Moreover, through the use of chlorosilanes, this scaffold permits the conversion of $Fe-N_2$ to $Fe\equiv N-NR_2$, modeling the first two steps in a Chatt-type mechanism. The generation and characterization of a parent $Fe\equiv N-NH_2$ unit, either directly from $Fe-N_2$ or otherwise, proved more challenging.

Recently, three Fe-based catalysts for N_2 reduction to NH_3 were reported by our laboratory.[12] These catalysts appear to be single-site[12a,13] and provide functional $Fe-N_2$ reduction systems for which systematic mechanistic studies can be conducted. In our original report,[12a] a new $S = 1/2$ species was generated by the low temperature addition of excess acid to $[(TPB)Fe(N_2)][Na(12\text{-crown-}4)_2]$ (**1**) in the absence of exogenous reductant. This doublet species was tentatively postulated to be the hydrazido(2−) complex $[(TPB)Fe\equiv N-NH_2][BAr^F_4]$ $(BAr^F_4 = (3,5\text{-}(CF_3)_2C_6H_3)_4B^-)$ (**2**),[12a] but several alternative structures such as those candidates depicted in Scheme 1 could not be excluded. Because **2** is a likely intermediate of catalytic nitrogen reduction by **1** (vide infra), its characterization is of primary interest.

Herein, we report combined EPR, ENDOR, and EXAFS spectroscopic studies that assign **2** as the parent hydrazido(2−) complex $[(TPB)Fe\equiv N-NH_2][BAr^F_4]$. ^{57}Fe Mössbauer studies indicate that this species constitutes a significant portion of the Fe-containing material upon exposure of **1** to acid. Finally, the geometric constraints provided by the spectroscopic data are corroborated by the optimized geometry of **2** obtained from Density Functional Theory (DFT) methods.

■ RESULTS AND DISCUSSION

Mixing of precatalyst **1** and 10 equiv of $HBAr^F_4\cdot2Et_2O$ in thawing 2-MeTHF solutions at −136 °C (Scheme 1) resulted in the disappearance of the dark red color characteristic of **1** and the formation of a brown-yellow solution. Analysis by CW X-band EPR indicates complete consumption of **1** and appearance of a new, more rhombic, $S = 1/2$ signal at 77 K (Figure 1B). Spin integration of the signal of **2** suggests a yield of 87(8)%. If stoichiometric acid is added to **1** at low temperature, rapid oxidation to neutral $S = 1$ $(TPB)Fe(N_2)$ with loss of 0.5 equiv H_2 occurs instead (eq 1) and no EPR signal is observed (Supporting Information).[12a]

$$\mathbf{1} + HBAr^F_4\cdot2Et_2O \rightarrow (TPB)Fe(N_2) + 0.5H_2 \qquad (1)$$

$$(TPB)Fe(N_2) + HBAr^F_4\cdot2Et_2O \rightarrow [(TPB)Fe]^+ + 0.5H_2 \qquad (2)$$

The signal for **2** can be generated, albeit at lower intensity, with as little as 2 equiv of acid. EPR spectra collected at 10 K reveal weak, complicated signals at low field that are consistent with one or more $S = 3/2$ species (Supporting Information), in addition to those stemming from **2**. The EPR spectrum of **2** is distinct from the more axial signature of **1** (Figure 1A) and it is also distinct from the previously reported EPR spectrum for $(TPB)Fe(N_2SiMe_3)$ (**3**).[11g] The fact that structurally characterized **3**, a model complex of the as yet uncharacterized complex '$(TPB)FeN_2H$', displays a more axial EPR spectrum than that of **2** suggests that **2** is electronically distinct from **3**, and by extension is unlikely to be the parent $(TPB)FeN_2H$ diazenido species (candidate **2′-E** in Scheme 1). Moreover, the requirement of ≥2 equiv of acid strongly suggests an alternative structure to **2′-E**.

Metal hydrazido(2−) complexes typically display substantial M−N multiple bonding, and are thus electronically similar to
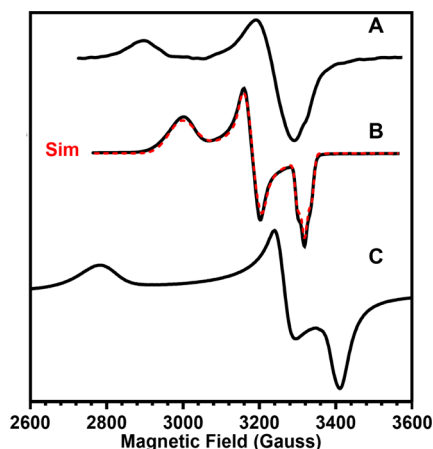

Figure 1. (A) The 77 K X-band (9.388 GHz) EPR of $[(TPB)Fe(N_2)][Na(12\text{-crown-}4)_2]$ (**1**). (B) The 77 K X-band (9.409 GHz) EPR after addition of 10 equiv of $HBAr^F_4\cdot2Et_2O$ to **1** to generate $[(TPB)Fe\equiv N-NH_2][BAr^F_4]$ (**2**). The parameters for the simulation of the spectrum are $g_1 = 2.222$, $g_2 = 2.091$, $g_3 = 2.006$, two ^{31}P nuclei coupling $A_3(^{31}P\alpha) = 64$ MHz, $A_3(^{31}P\beta) = 40$ MHz determined from ENDOR spectroscopy and third phosphorus of $A_3(^{31}P\lambda) \leq 20$ MHz; line broadening = 256, 113, and 41 MHz for g_1, g_2, and g_3, respectively. (C) The 77 K X-band (9.399 GHz) EPR of $[(TPB)Fe\equiv N-Ad][BAr^F_4]$ (**4**).

metal imido complexes.[5b,14] The cationic imido complex $[(TPB)Fe\equiv N-Ad][BAr^F_4]$ (**4**) is isoelectronic to $[(TPB)Fe\equiv N-NH_2][BAr^F_4]$, but was found to be thermally stable. This imido complex has been crystallographically characterized (Supporting Information) and also displays a rhombic EPR spectrum (Figure 1C). The rhombic EPR spectrum of **4** reflects a pseudotetrahedral iron center resulting from Fe−B elongation (Fe−B = 2.770 Å) as the iron center slips above the P_3 plane. This geometry should place an unpaired spin in a relatively nonbonding orbital arising from a $^2E_{dx^2-y^2,xy}$ state. This electronic structure is reminiscent of the ferrocenium cation and is also similar to various low spin $L_3Fe^{III}\equiv NR$ imides that have been previously described.[15,9d]

Fe−N triply bonded species supported by the TPB scaffold include $[(TPB)Fe\equiv N-Ad][BAr^F_4]$ (this work) and $(TPB)Fe\equiv N(4\text{-OMe-Ph})$.[11e] These species have characteristically short Fe−N distances of 1.660 and 1.668 Å, respectively. Structural data was sought for **2** to probe for an anticipated short $Fe\equiv N-NH_2$ triple bond. Iron K-edge extended X-ray absorption fine structure (EXAFS) data were collected and allowed for the observation of Fe-ligand distances in solution samples. These data were collected on frozen preparations (Supporting Information) of **2** in 2-MeTHF and are shown in Figure 2. Three pronounced peaks are observed in the Fourier transform spectrum, including one peak much shorter than expected for a singly bonded Fe−N pair. Indeed the EXAFS and Fourier transform spectra can be best fit with a short Fe−N distance of 1.64 Å and two Fe−P distances of 2.28 and 2.42 Å in a 1:2 ratio. Additionally, an Fe−B scattering path may be included in the fit at a distance of 2.67 Å, although convolution from the Fe−P scatterers makes this assignment tentative.

The observation of two different Fe−P scatterers for a complex with three phosphorus ligands can arise from various scenarios. If one assumes the EXAFS sample contains a single species, the two distances observed could correspond to a distorted structure with two long Fe−P distances and one short distance. A similar, though substantially lessened, distortion is
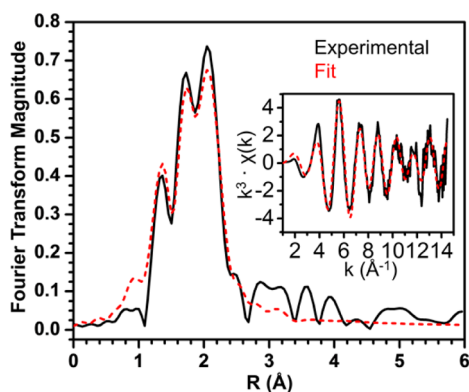
Figure 2. Fe K-edge Fourier transform of the EXAFS spectrum collected on a sample of **2**. Inset shows the EXAFS oscillations. Scatterer distances (Å) are Fe−P = 2.28, Fe−P = 2.42, Fe−N = 1.64, and Fe−B = 2.67 with the phosphines present in a 1:2 ratio. Full fit parameters may be found in the Supporting Information.

Figure 3. ^{57}Fe Mössbauer spectrum obtained by the reaction of ^{57}Fe-enriched $[(TPB)^{57}Fe(N_2)][Na(Et_2O)_x]$ with 5 equiv $HBAr^F_4 \cdot 2Et_2O$ in Et_2O at −110 °C. Data is shown as black dots, and the combined simulation is shown in red. The individual subspectra representing $(TPB)Fe(N_2)$, $[(TPB)Fe][BAr^F_4]$, and $[(TPB)Fe\equiv N-NH_2][BAr^F_4]$ (**2**) are shown in blue, orange, and green, respectively, and are offset for clarity. The spectrum was collected at 80 K in the presence of a 50 mT applied magnetic field to minimize line broadening (fast relaxation regime). Refer to the Supporting Information for simulation parameters and more detailed discussion.

observed in $[(TPB)Fe\equiv N-Ad][BAr^F_4]$. Alternatively, these disparate distances could arise from the presence of more than one species in the sample, each with a narrow distribution of Fe−P distances, a scenario that seems more likely based on the observation that oxidation of **1** by acid is a competing side reaction (eq 1). The apparently larger than expected Debye−Waller factor in the fitting for the Fe−N scatterer would thereby result from the presence of multiple species; the short and long Fe−P distances correspond closely to those observed in low-spin and high-spin iron complexes of the (TPB) ligand scaffold, which display variable Fe−N distances.[11f−h]

To further probe the possible presence of multiple iron species generated on addition of acid to **1** at low temperature, Mössbauer analysis of in situ generated solutions of **2** was undertaken. In brief, an ethereal solution of ^{57}Fe-enriched $[(TPB)^{57}Fe(N_2)][Na(Et_2O)_x]$ was frozen and then layered with excess $HBAr^F_4 \cdot 2Et_2O$ in Et_2O that was then also frozen. This sample was allowed to thaw to approximately −110 °C and mechanically stirred. The sample was then transferred to a Mössbauer cup chilled at 77 K for analysis. The Mössbauer spectrum of a representative sample is shown in Figure 3 and suggests the presence of three primary iron-containing species. Similarly prepared samples showed the same features but in variable ratios and hence caution must be exercised with respect to extrapolating the population of **2** in this specific Mössbauer sample relative to the population of **2** in independently prepared EXAFS and EPR samples. Nevertheless, the Mössbauer data confirm the presence of three (TPB)Fe-species generated under relatively comparable conditions. One of the three species present in the representative Mössbauer spectrum shown (∼20% of total Fe present; Supporting Information) can be definitively assigned as the neutral S = 1 Fe−N₂ adduct $(TPB)Fe(N_2)$ by comparison with an authentic sample (δ = 0.56 mm/s; ΔE_Q = 3.34 mm/s). The two other species are present in approximately equal amounts (40% each of total Fe). These two components can be simulated in multiple ways (see Supporting Information for a detailed discussion), but comparison of the simulation parameters with those of independently characterized, pure (TPB)Fe complexes suggests the simulation of Figure 3 to be the most reasonable. The simulation parameters suggest one component is the previously characterized S = 3/2 cation $[(TPB)Fe]^+$ (δ = 0.75 mm/s; ΔE_Q

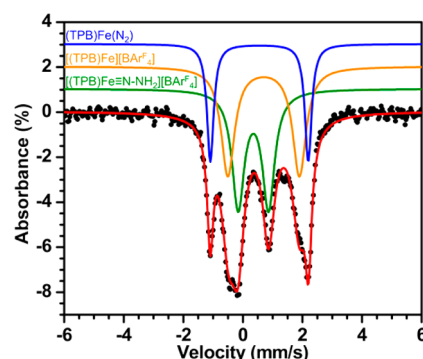= 2.55 mm/s);[16] the other by default is therefore the iron hydrazido(2−) cation **2** (δ = 0.35 mm/s; ΔE_Q = 1.02 mm/s).

The presence of $(TPB)Fe(N_2)$ and $[(TPB)Fe]^+$ in the sample is consistent with our previous finding that the addition of $HBAr^F_4 \cdot 2Et_2O$ to **1** leads to net oxidation of the complex to generate $(TPB)Fe(N_2)$ via loss of H_2.[12a] Likewise, $(TPB)Fe-(N_2)$ can be further oxidized to $[(TPB)Fe]^+$ via addition of $HBAr^F_4 \cdot 2Et_2O$ (eq 2, Supporting Information). In sum, the available Mössbauer data predicts that variously prepared samples of **2** may contain $(TPB)Fe(N_2)$ and $[(TPB)Fe]^+$, and this fact helps explain the additional P scatterer in the EXAFS data, as well as the larger than expected Fe−N Debye−Waller factor. As $(TPB)Fe(N_2)$ is EPR-silent, and $[(TPB)Fe]^+$ does not display EPR signals at 77 K, this Fe speciation is fully consistent with the clean spectrum observed by CW X-band EPR (Figure 1B).

While the aforementioned characterization data are most consistent with $[(TPB)Fe\equiv N-NH_2][BAr^F_4]$, the techniques used are not sensitive to the presence or location of the protons. As a direct probe of these protons, as well as other nuclei in **2**, we turned to electron nuclear double resonance (ENDOR) spectroscopy. This technique is particularly attractive because it selectively monitors S = 1/2 **2** regardless of the presence of the other species that complicate the EXAFS and Mössbauer analysis.

Figure 4 presents a 2D field-frequency pattern of ^{1}H Davies pulsed Q-band ENDOR spectra collected across the EPR envelope of **2**. In addition to ancillary ligand signals from weakly coupled protons with A < 4 MHz, the spectra show strongly coupled signals that arise from protonation of the N₂ ligand (Figure 4). The spectra collected at the "crystal-like" fields, g_1 and g_3, show two distinct ^{1}H doublets, $A_{g1}(^1H\alpha)$ ∼ 16 MHz, and $A_{g1}(^1H\beta)$ ∼ 10 MHz (Figure 4, blue and red, respectively), indicating the presence of two well-defined, inequivalent protons, consistent with assignment of **2** as exhibiting an unsymmetrically bound diprotonated (−N−NH₂) species, inconsistent with the proposed structures **2′-B** and **2′-E** (Scheme 1). Structure **2′-B** has two protons which are anticipated to be approximately equivalent with couplings
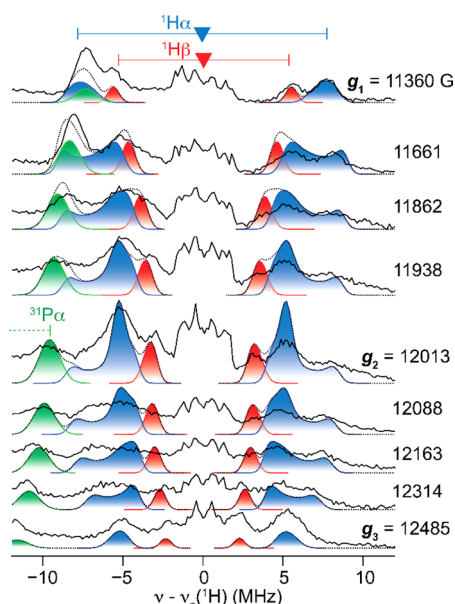
Figure 4. 2D field-frequency Q-band (35.049 GHz) Davies ENDOR pattern of **2** (*black solid*) collected at 2 K. $^1H\alpha$ (*blue*), **A** = [18.0, 10.5, 8.0] MHz, $\beta = 30°$; $^1H\beta$ (*red*), **A** = [11.5, 6.0, 4.5] MHz, $\beta = 0°$; ^{31}P (*green*), **A** = [43, 42, 40] MHz. Summed ENDOR simulation of $^1H\alpha$, $^1H\beta$, and ^{31}P is in black dashed line. *Conditions:* π = 60 ns; τ = 600 ns; T_{RF} = 30 μs; repetition time = 20 ms; RF frequency randomly hopped.

substantially larger than observed (see below), and structure **2'-E** should only have one proton signal.

As the magnetic field is increased, the $^1H\alpha$ feature splits, with the outer peak reaching a maximum ^1H coupling between g_1 and g_2 (11661 G), A_{max} = 18 MHz for $^1H\alpha$; with further increase in field, the pattern coalesces into the single doublet at g_3. The maximum coupling for a metal-bound hydride ($A_{max} \sim$ 40 MHz) is much larger,[17] inconsistent with structures **2'-C** and **2'-D**, Scheme 1. The $^1H\alpha$ pattern resembles that of a heme hydroperoxy Fe—O—OH proton,[18] an appealing analogy to the Fe—N—NH$_2$ unit in **2**, and those analyses provide a good starting point for analysis of the $^1H\alpha$ hyperfine tensor; simulation of the $^1H\alpha$ pattern (Figure 4, blue) yields a slightly rhombic tensor of **A** = +[18.0, 10.5, 8.0] MHz (see Figure 4 caption), whose anisotropic contribution corresponds to an Fe—Hα distance of $d > 3.1$ Å, with the Fe—Hα vector rotated away from g_1, which coincides approximately with the Fe—N bond and the molecular pseudo-C_3 axis.[19] In short, the analysis requires a nonlinear Fe—N—N geometry (Supporting Information Figure S8).

The smaller $^1H\beta$ coupling (Figure 4, red) exhibits a 2D pattern that can be described by a hyperfine tensor whose anisotropic contribution corresponds to an Fe—Hβ distance of $d > 3.5$ Å, with the Fe—Hβ vector along g_1 (the Fe—N bond). The absolute signs of the $^1H\alpha$, $^1H\beta$, couplings are implied by the assumption that the dominant anisotropic component is determined by through-space dipolar coupling, and were confirmed by the Variable Mixing Time (VMT) Pulsed ENDOR Saturation and Recovery (PESTRE) protocol (Supporting Information). The estimated Fe—$^1H\alpha/^1H\beta$ distances, along with the orientations of the hyperfine coupling tensors relative to **g**, imply that both protons have been added to the β-N of a bound N$_2$, to generate a bent Fe≡N—NH$_2$ moiety, with an Fe—N—N bond angle $\delta \sim 150°$ (Supporting Information). Notably, as indicated above, the metrical

parameters for the two protons are inconsistent with every other model visualized in Scheme 1.

Q-band $^{14/15}N$ ENDOR data was also acquired to further characterize the hydrazido ligand of **2** (Figure 5). A ^{15}N
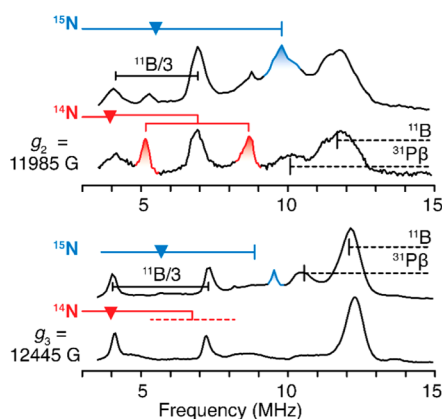

Figure 5. Q-band ($\sim$35.05 GHz) Davies pulsed ENDOR spectra of **2** collected at 2 K for each ^{14}N and ^{15}N isotopologues in red and blue, respectively. Observed $^{14/15}N$ coupling are Larmor centered (triangles) split by A and P for ^{14}N (goalposts). A stronger nitrogen coupling is observed in **2** following protonation of **1**. At g_2: $A_2(\mathbf{2}\text{-}^{15}N)$ = +9.0 MHz; $A_2(\mathbf{2}\text{-}^{14}N)$ = −6.4 MHz; $3P(\mathbf{2}\text{-}^{14}N)$ = 2.7 MHz. At g_3: $A_3(\mathbf{2}\text{-}^{15}N)$ = +8.0 MHz, but the corresponding $A_3(\mathbf{2}\text{-}^{14}N)$ = −5.7 MHz is possibly further quadrupole split and not observed. The ν_- feature of $a_{iso}(\mathbf{2}\text{-}^{11}B)$ = −8.7 MHz at $\sim$11 to 12 MHz. The features observed at 10.0 and 10.5 MHz at g_2 and g_3, respectively, are the ν_- of $a_{iso}(\mathbf{2}\text{-}^{31}P\beta)$ = 60 MHz. $^{11}B/3$: peaks at $\nu_B/3$, the third harmonic of ^{11}B nuclear Larmor frequency. Parameters: $\pi/2$ = 100 ns; τ = 600 ns; T_{RF} = 60 μs; repetition time = 20 ms.

ENDOR response is observed as a peak at ν_+ = +9.8 MHz (Figure 5), corresponding to $A_2(\mathbf{2}\text{-}^{15}N)$ = +9.0 MHz, $A_2(\mathbf{2}\text{-}^{14}N)$ = −6.4 MHz for the coordinated nitrogen (upon scaling by the gyromagnetic ratios of ^{14}N and ^{15}N ($\gamma \equiv g_n(^{14}N)/g_n(^{15}N) \equiv A(^{14}N)/A(^{15}N) = -0.71$)). The $\mathbf{2}\text{-}^{14}N$ ENDOR response has a quadrupole splitting of $3P$ = 2.7 MHz at g_2. Furthermore, the isotopically labeled ($\mathbf{2}\text{-}^{15}N$) sample has a resolved hyperfine coupling of $A_3(^{15}N)$ = +8.0 MHz near g_3. The corresponding ^{14}N ENDOR response of $\mathbf{2}\text{-}(^{14}N)$ is expected to have a coupling of $A_3(^{14}N)$ = −5.7 MHz, but is not observed. The additional quadrupole splitting of the ^{14}N at g_3 may orient **A** and **P** in such a manner that the quadrupole ENDOR response is too broad at g_3 and sharpest at g_2. No distinguishable nitrogen ENDOR features were observed at fields below g_2 for either $\mathbf{2}\text{-}(^{14}N)$ or $\mathbf{2}\text{-}(^{15}N)$, but the single-field three-pulse ESEEM spectrum of $\mathbf{2}\text{-}(^{14}N)$ (Supporting Information) is well simulated with a single ^{14}N tensor of $\mathbf{A}(\mathbf{2}\text{-}^{14}N)$ = −[4.34, 7.18, 6.22] MHz and quadrupole parameters of e^2qQ/h = 1.76 (P = 0.88 MHz) and rhombicity factor, η = 0.64, in excellent agreement with the observed P_2 = 0.90 MHz from ENDOR spectroscopy. The presence of quadrupole coupling with high rhombicity supports the idea of a nonlinear Fe—N—N linkage.

^{11}B ENDOR spectra of **2** (Supporting Information, Figures S10 and S11) show a coupling of $a_{iso} \sim$ −8.8 MHz, completing the characterization of the axial ligands to Fe. As shown in Supporting Information Figure S11, the ^{11}B nuclei exhibits a VMT-PESTRE response, typical of a nuclei with negative spin density and a negative **A**. Using the ^{11}B as a 'reference', the observed ^{14}N nuclei possesses negative spin density and $^1H\alpha$ and $^1H\beta$ both exhibit positive spin density. The negative spin

density observed on the ^{11}B and ^{14}N nuclei is a result of the spin-polarization of the Fe−B bond by the positive-spin density of the Fe center.

Finally, a nearly isotropic ^{31}P ENDOR signal from the phosphine ligand is simulated with $\mathbf{A}(^{31}P\alpha) = [43, 42, 40]$ MHz (Figure 4, green). Features of a second phosphine are observed in Figure 5, around 10.0−10.5 MHz and assigned as the ν_- transitions of ^{31}P doublet with $A \sim 60$ MHz; the ν_+ partner of this ^{31}P response unfortunately falls underneath the intense ENDOR response of weakly coupled solvent protons (^{1}H) (~55 MHz) (Supporting Information Figure S12). This observation of two ^{31}P couplings, one with $A_3(^{31}P\beta) \sim 64$ MHz the other with $A_3(^{31}P\alpha) = 40$ MHz by ENDOR spectroscopy correlates well with the simulation of the X-band EPR spectrum (Figure 1).

Computational studies were undertaken to compare the parameters of the theoretically predicted structure with those obtained spectroscopically. An optimized geometry (Supporting Information) of $[(TPB)Fe \equiv N-NH_2]^+$ was found, utilizing the core of $[(TPB)Fe \equiv NAd]^+$ for an initial guess. This geometry shows similar bonding metrics to those observed by EXAFS and ENDOR analysis. Thus, ENDOR requires diprotonation of the remote Nβ, while EXAFS requires a short Fe−Nα distance consistent with the calculated value 1.70 Å, and calculated Fe−P distances of 2.29, 2.31, and 2.36 Å (Figure 6A). The characteristically short Fe−N distance (i.e. ≤
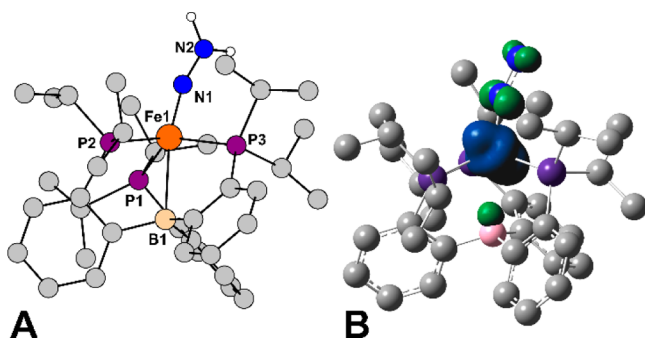

Figure 6. (A) Computed geometry for $[(TPB)Fe \equiv N-NH_2]^+$ and (B) spin density plot for $[(TPB)Fe \equiv N-NH_2]^+$. Both plots generated with the M06L functional with TZVP, SVP, and 6-31G(d) basis sets on Fe; P, B, N, C; and H, respectively.

1.7 Å) is consistently found when exploring a variety of functionals, while the Fe−P distances show slightly more variation (Supporting Information). In addition, the bending at Nα required for the interpretation of the ENDOR data is observed in the calculated gas-phase structure. Figure 6B depicts the predicted spin distribution in $[(TPB)Fe \equiv N-NH_2]^+$ suggesting that the majority of spin is carried by Fe with spin polarization observed on the NNH$_2$ and borane ligands, consistent with the ENDOR results. Other candidate structures for **2** were similarly optimized and found to be higher energy isomers. For example, a comparison of the energies of the hydrazido(2−) species versus a diazene isomer (Scheme 1, **2′-A**) shows that the assigned $[(TPB)Fe \equiv N-NH_2]^+$ isomer is lower in energy by 17.0 (BP86) or 8.2 (M06L) kcal/mol (Supporting Information). Taken together, the computational work is also consistent with the assignment of **2** as $[(TPB)Fe \equiv N-NH_2]^+$.

While **2** has been generated herein with excess acid at −136 °C in 2-MeTHF, N$_2$ reduction catalysis by **1** was originally

carried out at −78 °C in Et$_2$O by addition of acid followed by addition of reductant.[12a] As such, we sought to determine whether **2** could be detected in mixtures more relevant to catalysis, prior to the addition of the reductant. X-band EPR spectra of solutions prepared from the addition of acid to **1** at either −136 °C in 2-MeTHF or at −78 °C in Et$_2$O indicate that **2** is present in both preparations (Supporting Information, Figure S15). Furthermore, upon warming to −40 °C or to room temperature, both preparations show the growth of $S = 3/2$ signals concomitant with the decay of the signals of **2**. The identity of these $S = 3/2$ species is hard to determine due to convolution of the quartet signals. One such $S = 3/2$ species, $[(TPB)Fe(NH_3)]^+$, has been definitively assigned by inspection of the ^{1}H NMR spectrum of a similarly prepared mixture following warming to room temperature.[12a] Therefore, **2** decays at least in part to $[(TPB)Fe(NH_3)]^+$ upon warming even without exogenous reductant.

■ CONCLUSIONS

The combined spectroscopic data presented herein confirm the assignment of **2** as a $[(TPB)Fe \equiv N-NH_2]^+$ hydrazido(2-) complex. Alternative formulations for **2** can be excluded by the data presented. The observation of a short Fe−N distance by EXAFS spectroscopy conclusively excludes the two diazene formulations, **2′-A,B**, as well as **2′-E**. In addition, an η^1 diazene adduct (**2′-A**) should have two ^{1}H hyperfine couplings, but with one much stronger than the two observed. An η^2 diazene adduct (**2′-B**) is expected to have two ^{1}H couplings larger than observed. Hydride formulations (**2′-C, 2′-D**) are ruled out by the ^{1}H couplings and metric parameters already discussed. Finally, **2′-E** would have only one coupled proton.

To summarize, double protonation at the distal nitrogen, as invoked in a distal or Chatt type mechanism, is viable for this iron catalyst and likely occurs in the Fe-mediated N$_2$ fixation cycle catalyzed by **1** (Scheme 2). One or more downstream species arising from the decomposition of **2** involve higher spin ($S = 3/2$) species based on X-band EPR data (see Supporting Information). Plausible candidates for these $S = 3/2$ species include $[(TPB)Fe(NH_3)]^+$, $(TPB)Fe(NH_2)$, and $[(TPB)$-

Scheme 2. Distal, Alternating, and Hybrid Pathways[a]
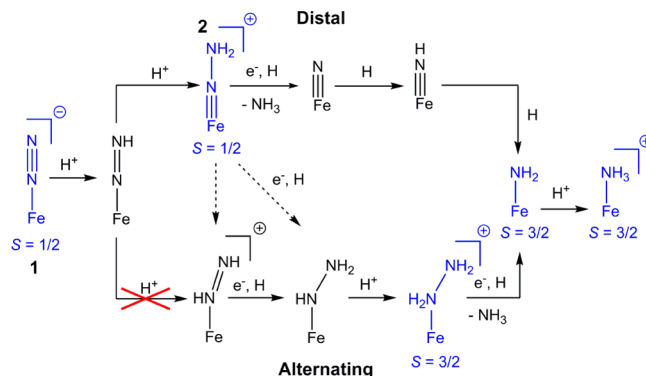
[a]Plausible scenarios that would transform $[Fe-N_2]^-$ catalyst **1** to $[Fe-NH_3]^+$ where $[Fe \equiv N-NH_2]^+$, **2**, is a key intermediate. Species shown in blue (along with spin states) have been experimentally characterized. *Top path* illustrates a limiting distal mechanism, *bottom path* an alternating mechanism, and the dotted arrows illustrate hybrid paths that could shuttle distal intermediate **2** to an alternating pathway that features late stage N−N cleavage. The order of protons, electrons, and/or H-atoms is provided for bookkeeping purposes only.

Fe]$^+$;[11h] these species, each of which is shown in blue in Scheme 2, are compatible with *both* distal and alternating scenarios. Another candidate $S = 3/2$ species is the hydrazine complex that would form on the alternating pathway, $[(TPB)Fe(N_2H_4)]^+$, which was previously characterized and shown to decompose to $[(TPB)Fe(NH_3)]^+$.[11h] A branching scenario whereby the distal intermediate **2** isomerizes to an alternate diazene structure, such as either **2′-A** or **2′-B** in Scheme 1, that then proceeds to $(TPB)Fe-N_2H_4^+$ as a later-stage intermediate of the alternating pathway, remains a mechanistic possibility.[7] Likewise, formal H atom addition to **2** at the Nα atom (Scheme 1) provides an alternative possible branching point from the distal to the alternating pathway. The key point we wish to underscore is that the observation of **2** is not incompatible with late stage N−N cleavage via a hydrazine intermediate.

Sorting out further mechanistic details for the present system warrants additional studies. But one conclusion is clear: an imide-like $[(TPB)Fe\equiv N-NH_2]^+$ species can be directly generated at low temperature by protonation of the Fe−N$_2$ catalyst precursor, and solutions of this species are known to decay to $[(TPB)Fe(NH_3)]^+$. This is a satisfying conclusion as it links the chemistry of iron-to-nitrogen multiple bonding to an N$_2$ fixation cycle. In this context, a conceptual parallel can be drawn to catalytic O$_2$ reduction wherein iron-to-oxygen multiply bonded species (e.g., Fe=O) are generated as intermediates.[20]

ASSOCIATED CONTENT

Ⓢ Supporting Information

Detailed experimental and spectroscopic data. The Supporting Information is available free of charge on the ACS Publications website at DOI: 10.1021/jacs.5b03432.

AUTHOR INFORMATION

Corresponding Authors
*jpeters@caltech.edu
*bmh@northwestern.edu
*limei.zhang@unl.edu

Present Addresses
#Department of Chemistry, Illinois College, 1101 West College Avenue, Jacksonville, IL, 62650, United States.
||Department of Biochemistry and Redox Biology Center, University of Nebraska—Lincoln, Lincoln, NE 68588, United States.

Author Contributions
§These authors contributed equally.

Notes
The authors declare no competing financial interest.

REFERENCES

(1) Burgess, B. K. *Chem. Rev.* **1990**, *90*, 1377−1406.
(2) (a) Kim, J.; Rees, D. C. *Science* **1992**, *257*, 1677−1682. (b) Einsle, O.; Tezcan, F. A.; Andrade, S. L. A.; Schmid, B.; Yoshida, M.; Howard, J. B.; Rees, D. C. *Science* **2002**, *297*, 1696−1700. (c) Spatzal, T.; Aksoyoglu, M.; Zhang, L. M.; Andrade, S. L. A.; Schleicher, E.; Weber, S.; Rees, D. C.; Einsle, O. *Science* **2011**, *334*, 940.
(3) (a) Burgess, B. K.; Lowe, D. J. *Chem. Rev.* **1996**, *96*, 2983−3011. (b) Eady, R. R. *Chem. Rev.* **1996**, *96*, 3013−3030.
(4) (a) Chatt, J.; Dilworth, J. R.; Richards, R. L. *Chem. Rev.* **1978**, *78*, 589−625. (b) Hidai, M.; Mizobe, Y. *Chem. Rev.* **1995**, *95*, 1115−1133.
(5) (a) Yandulov, D. V.; Schrock, R. R. *Science* **2003**, *301*, 76−78. (b) Arashiba, K.; Miyake, Y.; Nishibayashi, Y. *Nat. Chem.* **2011**, *3*, 120−125.
(6) (a) Armstrong, F. *Nature* **1985**, *317*, 576. (b) Pickett, C. J.; Talarmin, J. *Nature* **1985**, *317*, 652. (c) Leigh, G. J. *Science* **2003**, *301*, 55. (d) Schrock, R. R. *Nat. Chem.* **2011**, *3*, 95.
(7) Hoffman, B. M.; Dean, D. R.; Seefeldt, L. C. *Acc. Chem. Res.* **2009**, *42*, 609−619.
(8) (a) Bishop, P. E.; Jarlenski, D. M.; Hetherington, D. R. *Proc. Natl. Acad. Sci. U.S.A.* **1980**, *77*, 7342. (b) Schneider, K.; Gollan, U.; Dröttboom, M.; Selsemeier-Voigt, S.; Müller, A. *Eur. J. Biochem.* **1997**, *244*, 789. (c) Hinnemann, B.; Norskov, J. K. *Phys. Chem. Chem. Phys.* **2004**, *6*, 843.
(9) (a) Berry, J. F. *Comments Inorg. Chem.* **2009**, *30*, 28. (b) Scepaniak, J. J.; Young, J. A.; Bontchev, R. P.; Smith, J. M. *Angew. Chem., Int. Ed.* **2009**, *48*, 3158. (c) Crossland, J. L.; Tyler, D. R. *Coord. Chem. Rev.* **2010**, *254*, 1883−1894. (d) Saouma, C. T.; Peters, J. C. *Coord. Chem. Rev.* **2011**, *255*, 920−937. (e) Bowman, A. C.; Milsmann, C.; Bill, E.; Turner, Z. R.; Lobkovsky, E.; DeBeer, S.; Wieghardt, K.; Chirik, P. J. *J. Am. Chem. Soc.* **2011**, *133*, 17353. (f) King, E. R.; Hennessy, E. T.; Betley, T. A. *J. Am. Chem. Soc.* **2011**, *133*, 4917. (g) Kuppuswamy, S.; Powers, T. M.; Johnson, B. M.; Bezpalko, M. W.; Brozek, C. K.; Foxman, B. M.; Berben, L. A.; Thomas, C. M. *Inorg. Chem.* **2013**, *52*, 4802. (h) MacLeod, K. C.; Holland, P. L. *Nat. Chem.* **2013**, *5*, 559−565.
(10) For example see: (a) Field, L. D.; Guest, R. W.; Turner, P. *Inorg. Chem.* **2010**, *49*, 9086. (b) Crossland, J. L.; Balesdent, C. G.; Tyler, D. R. *Inorg. Chem.* **2011**, *51*, 439. (c) Rodriguez, M. M.; Bill, E.; Brennessel, W. W.; Holland, P. L. *Science* **2011**, *334*, 780. (d) Saouma, C. T.; Kinney, R. A.; Hoffman, B. M.; Peters, J. C. *Angew. Chem., Int. Ed.* **2011**, *50*, 3446−3449. (e) Balesdent, C. G.; Crossland, J. L.; Regan, D. T.; López, C. T.; Tyler, D. R. *Inorg. Chem.* **2013**, *52*, 14178. (f) Chiang, K. P.; AABellows, S. M.; Brennessel, W. W.; Holland, P. L. *Chem. Sci.* **2014**, *5*, 267. (g) Grubel, K.; Brennessel, W. W.; Mercado, B. Q.; Holland, P. L. *J. Am. Chem. Soc.* **2014**, *136*, 16807. (h) Rittle, J.; McCrory, C. C. L.; Peters, J. C. *J. Am. Chem. Soc.* **2014**, *136*, 13853.
(11) Betley, T. A.; Peters, J. C. *J. Am. Chem. Soc.* **2004**, *126*, 6252−6254. (b) MacBeth, C. E.; Harkins, S. B.; Peters, J. C. *Can. J. Chem.* **2005**, *83*, 332. (c) Peters, J. C.; Mehn, M. P. Bio-Organometallic Approaches to Nitrogen Fixation. In *Activation of Small Molecules*; Tolman, W. B., Ed.; Wiley-VCH: Weinheim, Germany, 2006; p 81. (d) Hendrich, M. P.; Gunderson, W.; Behan, R. K.; Green, M. T.; Mehn, M. P.; Betley, T. A.; Lu, C. C.; Peters, J. C. *Proc. Natl. Acad. Sci. U.S.A.* **2006**, *103*, 17107−17112. (e) Lee, Y.; Mankad, N. P.; Peters, J. C. *Nat. Chem.* **2010**, *2*, 558−565. (f) Moret, M.-E.; Peters, J. C. *Angew. Chem., Int. Ed.* **2011**, *50*, 2063−2067. (g) Moret, M.-E.; Peters, J. C. *J. Am. Chem. Soc.* **2011**, *133*, 18118−18121. (h) Anderson, J. S.; Moret, M.-E.; Peters, J. C. *J. Am. Chem. Soc.* **2013**, *135*, 534−537.
(12) (a) Anderson, J. S.; Rittle, J.; Peters, J. C. *Nature* **2013**, *501*, 84−87. (b) Creutz, S. E.; Peters, J. C. *J. Am. Chem. Soc.* **2013**, *136*, 1105−1115. (c) Ung, G.; Peters, J. C. *Angew. Chem., Int. Ed.* **2015**, *54*, 532.
(13) While catalysis appears to be mediated by monometallic species, we cannot exclude a role for bi- or multimetallic intermediates.
(14) (a) Hidai, M.; Kodama, T.; Sato, M.; Harakawa, M.; Uchida, Y. *Inorg. Chem.* **1976**, *15*, 2694. (b) Gebreyes, K.; Zubieta, J.; George, T. A.; Koczon, L. M.; Tisdale, R. C. *Inorg. Chem.* **1986**, *25*, 405. (c) Yandulov, D. V.; Schrock, R. R. *Inorg. Chem.* **2005**, *44*, 1103.

(15) Brown, S. D.; Betley, T. A.; Peters, J. C. *J. Am. Chem. Soc.* **2002**, *125*, 322.

(16) While we favor [(TPB)Fe]$^+$, structurally and electronically similar $S = 3/2$ species that feature a weakly bound axial ligand, including [(TPB)Fe(NH$_3$)][BAr$^F_4$] and [(TPB)Fe(N$_2$H$_4$)][BAr$^F_4$], cannot be strictly excluded as alternative candidates.

(17) Kinney, R. A.; Hetterscheid, D. G. H.; Hanna, B. S.; Schrock, R. R.; Hoffman, B. M. *Inorg. Chem.* **2010**, *49*, 704.

(18) (a) Davydov, R.; Kofman, V.; Fujii, H.; Yoshida, T.; Ikeda-Saito, M.; Hoffman, B. M. *J. Am. Chem. Soc.* **2002**, *124*, 1798. (b) Davydov, R.; Makris, T. M.; Kofman, V.; Werst, D. E.; Sligar, S. G.; Hoffman, B. M. *J. Am. Chem. Soc.* **2001**, *123*, 1403.

(19) (a) McNaughton, R. L.; Chin, J. M.; Weare, W. W.; Schrock, R. R.; Hoffman, B. M. *J. Am. Chem. Soc.* **2007**, *129*, 3480. (b) McNaughton, R. L.; Roemelt, M.; Chin, J. M.; Schrock, R. R.; Neese, F.; Hoffman, B. M. *J. Am. Chem. Soc.* **2010**, *132*, 8645. (c) Kinney, R. A.; McNaughton, R. L.; Chin, J. M.; Schrock, R. R.; Hoffman, B. M. *Inorg. Chem.* **2011**, *50*, 418. (d) Lee, Y.; Kinney, R. A.; Hoffman, B. M.; Peters, J. C. *J. Am. Chem. Soc.* **2011**, *133*, 16366. (e) Gunderson, W. A.; Suess, D. L. M.; Fong, H.; Wang, X.; Hoffmann, C. M.; Cutsail, G. E., III; Peters, J. C.; Hoffman, B. M. *J. Am. Chem. Soc.* **2014**, *136*, 14998. (f) Cutsail, G. E., III; Stein, B. W.; Subedi, D.; Smith, J. M.; Kirk, M. L.; Hoffman, B. M. *J. Am. Chem. Soc.* **2014**, *136*, 12323.

(20) Nam, W. *Acc. Chem. Res.* **2007**, *40*, 522.